Available online at www.sciencedirect.com
SCIENCE DIRECT®
International Journal of Heat and Fluid Flow 25 (2004) 393–403
International Journal of HEAT AND FLUID FLOW
www.elsevier.com/locate/ijhff

DNS of velocity and thermal fields in turbulent channel flow with transverse-rib roughness

Yasutaka Nagano [a,*], Hirofumi Hattori [a], Tomoya Houra [b]

[a] Department of Mechanical Engineering, Nagoya Institute of Technology, Gokiso-cho, Showa-ku, Nagoya 466-8555, Japan
[b] Department of Environmental Technology, Nagoya Institute of Technology, Gokiso-cho, Showa-ku, Nagoya 466-8555, Japan

Abstract

A detailed knowledge of both velocity and thermal fields in wall turbulence disturbed by a row of ribs on the wall is important for clarifying the chief factors of fluid and thermal dynamics related to the control of heat transfer. In this study, in order to elucidate the effects of roughness on the statistical quantities in the velocity and thermal fields, direct numerical simulations (DNS) of heat transfer in turbulent channel flows with transverse-rib roughness have been performed by varying their spacing, width and height, in which the turbulent heat transfer with k-type and d-type roughness walls are simulated. It is found that since turbulent mixing is promoted by arranging ribs, the distributions of mean velocity and temperature become markedly asymmetric. Systematic variations of secondary flow patterns between ribs are clearly identified. The best heat transfer performance is found to be obtained with the k-type roughness.

Keywords: Turbulence; Heat transfer augmentation; Transverse-rib roughness; Direct numerical simulation

1. Introduction

Arranging roughness elements or protuberances on the heat transfer surface, which is expected to promote near-wall turbulence and improve the efficiency of convective heat transfer, has been applied to many kinds of industrial machinery, including heat exchangers and turbine blades. However, from the standpoint of energy efficiency, these roughness elements have the drawback of causing drag while increasing heat transfer. Therefore, a detailed knowledge of both velocity and thermal fields in wall turbulence disturbed by the elements of ribs on the wall is important for clarifying the chief factors of fluid and thermal dynamics related to the control of heat transfer. Experimental investigations for turbulent channel flows with transverse-rib roughness have been reported by numerous researchers (e.g., Perry et al., 1969; Antonia and Luxton, 1971, 1972; Hanjalić and Launder, 1972; Bakken and Krogstad, 2001; Liou et al., 1993). However, it is difficult to measure in detail the characteristics of turbulent flow near the rough wall including transport of heat. On the other hand, the rapid progress in high-performance computers has promoted direct numerical simulation (DNS), which provides us an accurate solution of the governing equations without introducing assumptions. Moreover, DNS serves to increase an understanding of the generation of turbulence and its maintenance mechanisms including the thermal field. Numerical studies of the velocity field in the rib-roughened channel flow have been recently reported (Cui et al., 2003; Ashrafian and Andersson, 2003; Leonardi et al., 2003). Although an analysis has been made of turbulent thermal fields with roughness using DNS (Miyake et al., 2000), there has been no systematic study on the effects of the height and spacing of the roughness elements.

In the present study, to obtain detailed knowledge of the effects of the roughness elements on both velocity and thermal fields in the near-wall region, we performed a DNS using finite-difference methods, making it relatively easy to change the boundary conditions. In a DNS, the periodic transverse-rib roughnesses are arranged in the streamwise direction, and the spacing, width and height are systematically varied. The flow fields are thus constructed to simulate so-called k- and

* Corresponding author. Tel.: +81-52-735-5325; fax: +81-52-735-5359.
E-mail address: nagano@heat.mech.nitech.ac.jp (Y. Nagano).

0142-727X/$ - see front matter © 2004 Elsevier Inc. All rights reserved.
doi:10.1016/j.ijheatfluidflow.2004.02.011

Nomenclature

$\overline{C_{fr}}$	friction coefficient at rough wall, $2\overline{\tau_{wr}}/(\rho\langle U\rangle_r^2)$
C_{fs}	friction coefficient at smooth wall, $2\tau_{ws}/(\rho\langle U\rangle_s^2)$
d	distance between rough wall and location where mean velocity becomes maximum
H	height of rib roughness (see Fig. 1)
II	fluctuation of the second invariant of deformation tensor
k	turbulent kinetic energy, $\overline{u_iu_i}/2$
$\overline{Nu}_r$	Nusselt number at rough wall, $2\overline{q_{wr}}d/[(T_h-\langle T\rangle_r)\lambda]$
Nu_s	Nusselt number at smooth wall, $2q_{ws}(2\delta-d)/[(\langle T\rangle_s-T_c)\lambda]$
p	pressure
Pr	Prandtl number
Pr_t	turbulent Prandtl number
$\overline{q_{wr}}$, q_{ws}	heat fluxes at rough and smooth walls
Re_r	Reynolds number on rough-wall side, $2\langle U\rangle_r d/\nu$
Re_s	Reynolds number on smooth-wall side, $2\langle U\rangle_s(2\delta-d)/\nu$
$Re_{\tau 0}$	Reynolds number based on friction velocity and channel half width, $u_{\tau 0}\delta/\nu$
S	spacing between consecutive ribs (see Fig. 1)
$\overline{St}_r$	Stanton number at rough wall, $\overline{Nu}_r/(PrRe_r)$
t	time
T_h, T_c	temperatures at rough and smooth walls
$\langle T\rangle_r$	bulk mean temperature on rough-wall side, $\int_0^d \overline{U}(T_h-\overline{T})\,dy/(\langle U\rangle_r d)$
$\langle T\rangle_s$	bulk mean temperature on smooth-wall side, $\int_d^{2\delta}\overline{U}(T_h-\overline{T})\,dy/[\langle U\rangle_s(2\delta-d)]$
$\overline{U}$	mean velocity in the x-direction
U_m	bulk mean velocity, $\int_0^{2\delta}\overline{U}\,dy/(2\delta)$
$\langle U\rangle_r$	bulk mean velocity on rough-wall side, $\int_0^d\overline{U}\,dy/d$
$\langle U\rangle_s$	bulk mean velocity on smooth-wall side, $\int_d^{2\delta}\overline{U}\,dy/(2\delta-d)$
u_i	fluctuating velocity component in x_i direction
u, v, w	fluctuating velocity components in x-, y- and z-directions
$u_{\tau 0}$	mean friction velocity calculated from pressure gradient, $\sqrt{-(\delta/\rho)(d\bar{p}/dx)}$
u_τ	friction velocity, $\sqrt{\tau_w/\rho}$
W	crest width of rib roughness (see Fig. 1)
x_i	spatial coordinate in the i direction
x, y, z	streamwise, wall-normal and spanwise coordinates

Greeks

δ	channel half width
ΔT_w	temperature difference between rough and smooth walls, T_h-T_c
λ	thermal conductivity
ν	kinematic viscosity
$\overline{\Theta}$	mean temperature difference from rough-wall temperature, $T_h-\overline{T}$
θ	fluctuating temperature difference, $\Theta-\overline{\Theta}=\overline{T}-T$
ρ	density
τ_w	wall shear stress
Φ_{ij}	pressure–strain term, $\overline{\frac{p}{\rho}\left(\frac{\partial u_i}{\partial x_j}+\frac{\partial u_j}{\partial x_i}\right)}$

Subscripts and superscripts

$(\,)_0$	averaged value of both walls or predicted value from correlation curve
$(\,)_r$	value on rough-wall side
$(\,)_{rms}$	rms intensity
$(\,)_s$	value on smooth-wall side
$\overline{(\,)}$	ensemble averaged value
$(\,)^+$	normalization by inner variables, u_τ and ν

d-type roughness. We attempted to obtain the optimal rib arrangement to promote heat transfer, and investigated the turbulence thermal structure from various viewpoints.

2. Numerical procedure

Fig. 1 shows a schematic of the channel with transverse-rib roughness and the coordinate system used in the present study. The origin of the coordinate axes is located in the middle of the enclosure between the ribs. Table 1 shows some details of the computational methods. DNS based on the finite-difference method was carried out with a constant mean pressure gradient to balance the wall-shear stress on both walls. A fully consistent and conservative finite-difference method is used for the convective term of the Navier–Stokes equation (Kajishima, 1999). The number of grid points in the y-direction in the enclosure is 36 for Cases 1, b and c, and 18 for Cases 2 and 3. In order to solve the Poisson equation for the pressure, the standard SOR method is applied and the over-relaxation coefficient is set to 1.5. The time advancement is $\Delta t^* = 1\times 10^{-4}$, and the total time steps needed for the statistical quantities to converge reasonably are 300,000 for each case. The numerical scheme used in this study is validated by comparing the statistical quantities, including the bud-

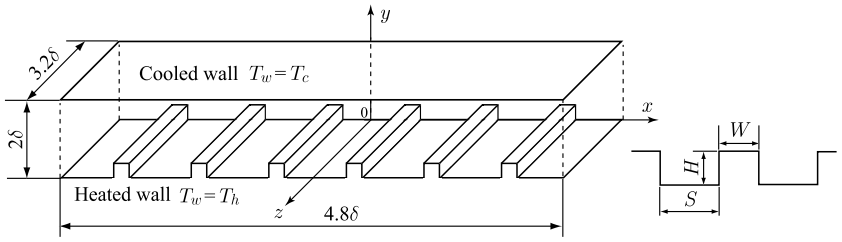

Fig. 1. Channel with transverse-rib roughness and coordinate system.

Table 1
Computational methods

Channel with transverse-rib roughness		
Grid		Staggered grid
Coupling algorithm		Fractional step method
Time advancement	Conductive term	Crank–Nicolson method
	Other terms	Adams–Bashforth method
Spatial scheme		Second-order central difference
Computational volume		$4.8\delta \times 2\delta \times 3.2\delta$
Grid points ($x \times y$ (rib outside + rib inside) $\times z$)		$192 \times (96 + 36$ or $18) \times 96$
Grid resolution		$\Delta x^* = 3.75$ $\Delta y^* = 0.30$–6.50 $\Delta z^* = 5.0$

get of the turbulent kinetic energy, in the plane channel flow with those calculated by Nagano and Hattori (2003), employing a spectral method.

The velocity field is governed by the incompressible Navier–Stokes equation without buoyancy and the continuity equation. They are given as follows:

$$\frac{\partial u_i^*}{\partial t^*} + u_j^* \frac{\partial u_i^*}{\partial x_j^*} = -\frac{\partial p^*}{\partial x_i^*} + \frac{1}{Re_{\tau 0}} \frac{\partial^2 u_i^*}{\partial x_j^* \partial x_j^*} + \Pi_1^*, \tag{1}$$

$$\frac{\partial u_i^*}{\partial x_i^*} = 0, \tag{2}$$

where Π_1^* is the non-dimensionalized constant mean pressure gradient to maintain a flow. The superscript * indicates the normalization by the total mean friction velocity $u_{\tau 0}$ defined later and the channel half width δ. The boundary conditions for the velocity field are periodic in x- and z- directions and no-slip on the walls. For the thermal field, it is assumed that the averaged heat fluxes on both walls, i.e., heat input and output, balance each other. Thus, the temperatures on the rough and smooth walls are fixed to T_h and T_c, respectively. The temperature is non-dimensionalized with the temperature difference $\Delta T_w = T_h - T_c$, and then defined as $\theta^* = (T_h - T)/\Delta T_w$. The boundary conditions of the temperature θ^* are as follows:

$$\begin{cases} \theta^* = 0 & \text{(rough wall)}, \\ \theta^* = 1 & \text{(smooth wall)}. \end{cases} \tag{3}$$

Table 2
Rib parameters

	H	W	S	Roughness type
Case 1	0.2δ	0.2δ	0.6δ	k-type
Case 2	0.1δ	0.2δ	0.6δ	
Case 3	0.05δ	0.2δ	0.6δ	
Case b	0.2δ	0.4δ	0.4δ	d-like type
Case c	0.2δ	0.2δ	0.2δ	

The energy equation governing the thermal field is as follows:

$$\frac{\partial \theta^*}{\partial t^*} + u_j^* \frac{\partial \theta^*}{\partial x_j^*} = \frac{1}{PrRe_{\tau 0}} \frac{\partial^2 \theta^*}{\partial x_j^* \partial x_j^*}. \tag{4}$$

The calculation conditions are: Reynolds number, $Re_{\tau 0} = 150$; and Prandtl number, $Pr = 0.71$, assuming the working fluid to be air.

Five types of wall roughness are arranged as listed in Table 2. According to the classification of roughness (Perry et al., 1969; Townsend, 1976), Case 1 belongs to k-type roughness, and is similar shape to the experiment of Hanjalić and Launder (1972). In Case 2 the ribs are set to half the height of Case 1, and in Case 3, the height is set to half the height of Case 2. In the k-type roughness, the effect of the roughness is expressed in terms of the roughness Reynolds number, $H^+ = u_\tau H/\nu$. In Cases b and c, the height of the ribs is set the same as in Case 1, though the spacing of the ribs is varied systematically. Case c belongs to d-type roughness, in which the effect of the roughness cannot be expressed by H^+. On the other hand, Case b is not regarded as the "exact" d-type, but d-like type roughness. It should be noted that the two kinds of roughness elements, i.e., k and d types, are the extreme versions and intermediate forms can exist (Townsend, 1976).

3. Results and discussion

3.1. Heat transfer and skin friction coefficients

Figs. 2 and 3, respectively, show the skin friction coefficient and the Nusselt number against the Reynolds number. By taking into account the asymmetry (Kasagi

and Nishimura, 1997) in the flow field disturbed by the ribs, the skin friction coefficient and the Nusselt number at the rough wall are defined as follows:

$$\overline{C_{\rm fr}} = \frac{2\overline{\tau_{\rm wr}}}{\rho\langle U\rangle_{\rm r}^2}, \quad \overline{Nu}_{\rm r} = \frac{2\overline{q_{\rm wr}}d}{(T_{\rm h} - \langle T\rangle_{\rm r})\lambda}, \tag{5}$$

where d indicates the distance between the wall and the location where the mean velocity becomes maximum, and $\langle\ \rangle$ denotes the bulk mean over the distance d. At the smooth wall, they are similarly defined as follows:

$$C_{\rm fs} = \frac{2\tau_{\rm ws}}{\rho\langle U\rangle_{\rm s}^2}, \quad Nu_{\rm s} = \frac{2q_{\rm ws}(2\delta - d)}{(\langle T\rangle_{\rm s} - T_{\rm c})\lambda}. \tag{6}$$

The wall shear stress, $\tau_{\rm ws}$, at the (upper) smooth wall is estimated directly by the mean velocity gradient on the wall and then, $\overline{\tau_{\rm wr}}$ at the (lower) rough wall is calculated from the balance of the imposed pressure gradient,

$$\overline{\tau_{\rm wr}} = -2\delta\frac{{\rm d}\bar{p}}{{\rm d}x} - \tau_{\rm ws} = 2\tau_{\rm w0} - \tau_{\rm ws}. \tag{7}$$

The above-defined wall shear stress at the rough wall, $\overline{\tau_{\rm wr}}$, includes the pressure drag (form drag) $\tau_{\rm wp}$, as well as the viscous drag, $\tau_{\rm wv}$,

$$\overline{\tau_{\rm wr}} = \tau_{\rm wp} + \tau_{\rm wv}. \tag{8}$$

On the other hand, because the fully developed state is assumed for the thermal condition in the present study, there is no increase in the enthalpy of the flowing fluid in the streamwise direction. Thus, the overall heat flux at the rough wall, $\overline{q_{\rm wr}}$, is equal to the absolute value of that at the smooth wall, $q_{\rm ws}$, which can be estimated directly by the mean temperature gradient on the wall. In order to compare the results with the correlation curve by Kays and Crawford (1993) for the pipe flow, the length scales of the Reynolds and Nusselt numbers are doubled in Fig. 3. In those figures, the DNS results in the plane channel flow ($Re_\tau = 150$) calculated by the spectral method (Nagano and Hattori, 2003) are also included to compare with the results of the present DNS.

From Figs. 2 and 3, it can be seen that the skin friction coefficient and the Nusselt number at the rough wall become very large in comparison with those at the corresponding smooth wall, where these quantities are well represented by the correlation curves. Moreover, from Fig. 2, even though the imposed pressure gradient is the same as in the smooth wall, the rib decreases the bulk mean velocity, so the Reynolds number heavily depends on the rib configuration; in Case 1, where the rib is highest in the k-type roughness walls, the Reynolds number is the smallest among them. In the present study, Case 3 is found to be the lowest in drag. On the other hand, in the d-like type roughness (Cases b and c), the heat transfer augmentation is smaller than that in the k-type roughness with the same roughness height (Case 1).

Table 3 shows the Stanton number, the skin friction coefficient and the Nusselt number, which are divided by the estimated smooth-wall values from the respective correlation curve (Dean, 1978; Kays and Crawford, 1993) for the same Reynolds number. In the k-type classification, Case 1 enhances heat transfer most. However, from the viewpoint of the heat transfer characteristic including the drag, if we compare the Stanton number divided by the skin friction coefficient $\overline{St}_{\rm r}/\overline{C_{\rm fr}}$, from Table 3, Case 1 enhances the heat transfer more than the smooth wall, but the overall characteristics of heat transfer do not improve because of the large drag. However, Case 3, the k-type with the lowest ribs, promotes the heat transfer with very low drag. This case is the most efficient from the standpoint of overall heat transfer performance including the drag. In the d-like type roughness, the heat transfer characteristic cannot be improved regardless of the rib spacing. The stagnation region in the enclosure becomes larger than that in the k-type roughness (not shown here), and the deteri-

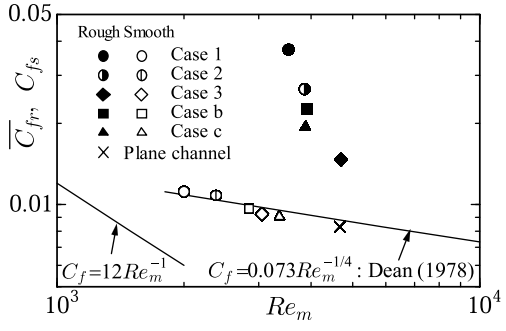

Fig. 2. Distributions of skin friction coefficients.

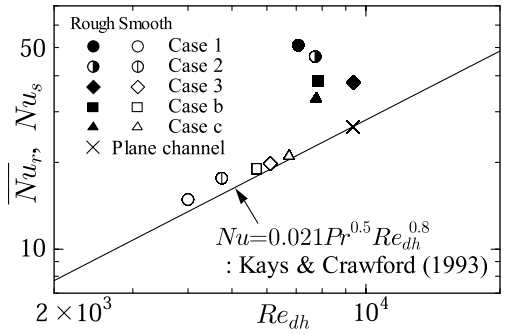

Fig. 3. Distributions of Nusselt numbers.

Table 3
Coefficients for heat-transfer rate at rough wall

	$(\overline{St}_{\rm r}/\overline{C_{\rm fr}})/(St_0/C_{f0})$	$\overline{C_{\rm fr}}/C_{f0}$	$\overline{Nu}_{\rm r}/Nu_0$
Case 1	0.61	3.93	2.41
Case 2	0.71	2.87	2.04
Case 3	0.85	1.66	1.42
Case b	0.69	2.44	1.67
Case c	0.69	2.10	1.46

oration in heat transfer has become pronounced there. Thus, in the following, we discuss the effects of the height of the rib on the statistical characteristics of thermal property in the k-type roughness, which includes a rib configuration which promotes the heat transfer.

3.2. Velocity and thermal fields around the rib

To visualize the velocity and thermal fields around the rib, Figs. 4 and 5 show the mean streamlines estimated from the mean velocity profiles and contour lines of the mean temperature distributions. The averages are taken only with respect to the spanwise direction in these figures. Two-dimensional vortices exist in the enclosures between the ribs in Cases 1 and 2, and their shapes are different in each case. In Case 1, the center of the two-dimensional vortex is biased to the upstream side of the rib and becomes asymmetric, whereas in Case 2 the center of the vortex is biased to the downstream side of the rib. Moreover, in Case 3, the small two-dimensional vortices are located on both sides of the rib, and the flow reattachment is seen in the enclosure.

On the other hand, from the contour lines of the mean temperature, around the front corner of the rib, the spacing between the lines becomes smaller, making for very active heat transfer there. In the enclosure between the ribs, the contour lines are distorted corresponding to the streamlines and are not parallel to the bottom wall. Especially, in Case 3, it is confirmed that the mean temperature contour lines are densely distributed, causing more enhanced heat transfer. On the upstream side of the ribs, the wavy patterns of temperature can be seen, a phenomenon also observed by an experiment using holographic interferograms as shown in Fig. 6 (Liou et al., 1993). Liou et al. obtained the figure as an instantaneous snapshot of temperature variations, but it is considered to be averaged with respect to the spanwise direction as in Fig. 5. Thus, the phenomenon is regarded as a characteristic specific to a temperature field near the upstream side of the rib.

Figs. 7 and 8 show the local skin friction coefficient, $C_{\mathrm{fr}}(x)[= 2\tau_{\mathrm{wv}}(x)/\rho\langle U\rangle_{\mathrm{r}}^2]$ and the local Nusselt number, $Nu_{\mathrm{r}}(x)[= 2q_{\mathrm{wr}}(x)d/(T_{\mathrm{h}} - \langle T\rangle_{\mathrm{r}})\lambda]$ along the bottom of the enclosure and the crest on the rough wall, divided by the values on the smooth wall estimated from the respective correlation curve. These mean quantities are obtained by averaging with respect to time, the spanwise direction and the streamwise period of the rib roughness. The local wall shear stress, $\tau_{\mathrm{wv}}(x)$, and wall heat flux, $q_{\mathrm{wr}}(x)$, are estimated directly from the gradients of mean velocity and temperature, respectively. Thus, the local shear stress shown in Fig. 7 does not include the pressure drag (see Eq. (8)). By averaging the local wall shear stress along the bottom of the enclosure and the crest in the x-direction, the contributions of the viscous drag to the total drag of the rough-wall side are estimated at 4.5%, 1.1% and 20.8%, in Cases 1, 2 and 3, respectively.

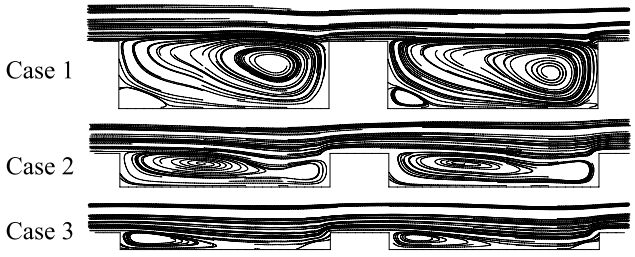

Fig. 4. Streamlines of mean velocity averaged in the spanwise direction. Flow is left to right.

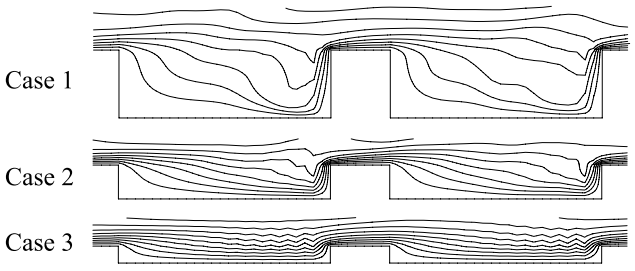

Fig. 5. Contour lines of mean temperature averaged in the spanwise direction. The interval between successive contour level is 0.02. Flow is left to right.

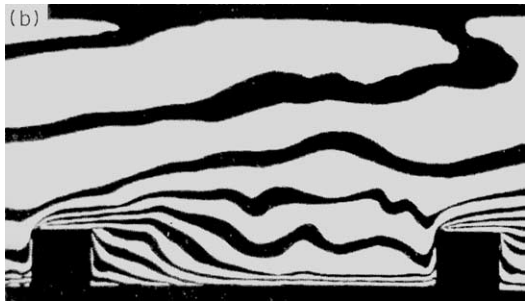

Fig. 6. Temperature distributions from holographic interferogram (Liou et al., 1993).

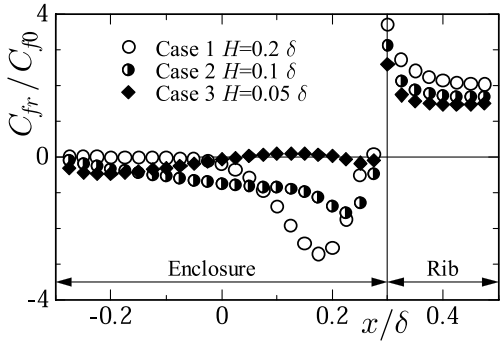

Fig. 7. Profiles of local skin friction coefficients around rib along the horizontal wall with $x = 0$ at the middle of the enclosure.

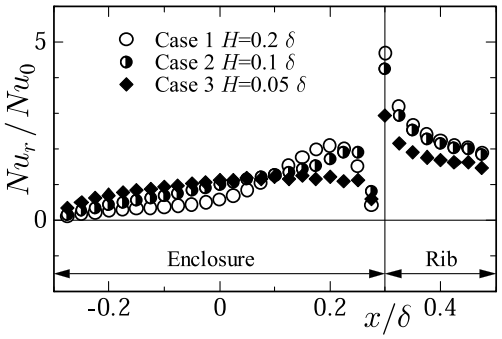

Fig. 8. Profiles of local Nusselt number around rib along the horizontal wall with $x = 0$ at the middle of the enclosure.

In Case 2, because the negative contribution to the viscous drag from the two-dimensional vortices in the enclosure nearly balances with the positive contribution on the rib crest, the ratio of the pressure drag to the viscous drag is very large, i.e., $\tau_{wp}/\tau_{wv} = 21.2$, 91.5 and 3.8 for Cases 1, 2 and 3, respectively. It might be worthwhile to clarify the relationship between the heat transfer augmentation and the drag ratio, which closely relates to the mixing in the core region. Ashrafian and Andersson (2003) reported the contribution of the viscous drag to the total drag was 2.5%, in their DNS calculation of the rib-roughened channel flow (the pitch to the height ratio, $(S + W)/H$, is 8, $Re_{\tau 0} = 400$). Recently, Leonardi et al. (2003) have systematically investigated the effects of the pitch to the height ratio on the contributions from the viscous and pressure drags. They reported that the total drag is determined almost entirely by the pressure drag when the ratio is within the range from 6 to 20.

From Fig. 7, the local skin friction coefficient becomes minimum in the enclosure and maximum at the front corner of the rib in Cases 1 and 2. On the other hand, in Case 3, although the local skin friction coefficient takes the maximum at the front corner of the rib, both a large overall decrease and a local peak in the enclosure cannot be seen; but it changes sign in the enclosure. The reattachment point (defined as the location where the local skin friction coefficient becomes zero) is located at $x/\delta = 0.04$; thus the forward flow region is observed over $0.04 < x/\delta < 0.21$ until separation occurs in the enclosure between the ribs.

The local Nusselt numbers in Cases 1 and 2 distribute similarly to the *absolute value* of the local skin friction coefficient. However, in Case 3, the Nusselt number increases over the entire region in the enclosure. This situation is also observed near the reattachment region of the backward-facing step flows (Vogel and Eaton, 1985), and it is reported that the heat transfer coefficient reaches maximum there. Similarly, the local Nusselt number increases in approaching the reattachment point $x/\delta = 0.04$ and the following forward flow region $(0.04 < x/\delta < 0.21)$. From the above results, it is confirmed that in Case 3, the heat transfer is promoted, yet with only a relatively small increase in the drag.

3.3. Statistical characteristics of velocity field and turbulent structures

It is assumed that in a velocity field of a channel flow with a rib surface, the flow motions in the enclosure between the ribs strongly affect the flow field above the ribs. Figs. 9 and 10 show the mean velocity and Reynolds shear stress profiles in Case 1. We examined the various ways of averaging, e.g., average over the x–z plane, spanwise average at the middle of the enclosure $(x/\delta = 0)$ and at the rib crest $(x/\delta = 0.4)$. As seen from these figures, the differences cannot be seen along the streamwise direction except near the roughness element. Thus, in the following, the statistical quantities of turbulence in the middle of the enclosure $(x/\delta = 0)$ are discussed.

Fig. 11 shows the mean velocity normalized by the bulk velocity U_m. Because of the effects of the rib, it is observed that the velocity decreases on the rough-wall side. The corresponding distributions of the Reynolds shear stress and turbulent kinetic energy are shown in Figs. 12 and 13. As the rib height increases, turbulence is promoted, and both the Reynolds shear stress and the turbulence energy increase near the wall. This affects the region over the center of the channel. However, in the near-wall region of the opposite wall, there is only a small effect, in comparison with the results for the plane channel flow. Despite the negative value of the velocity gradient near the wall in the enclosure as seen in Fig. 11, the Reynolds shear stress takes a positive value, thus confirming the occurrence of counter gradient diffusion. Because the production of the Reynolds shear stress is mainly maintained with the pressure–strain correlation and the pressure diffusion, no production from the mean shear is observed. An experimental study (Hanjalić and Launder, 1972) indicated that the place where the Reynolds shear stress becomes zero and the mean velocity becomes maximum is different. However, the difference

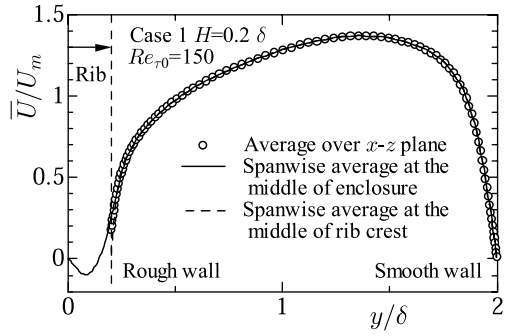

Fig. 9. Profiles of mean velocity calculated by various ways of averaging.

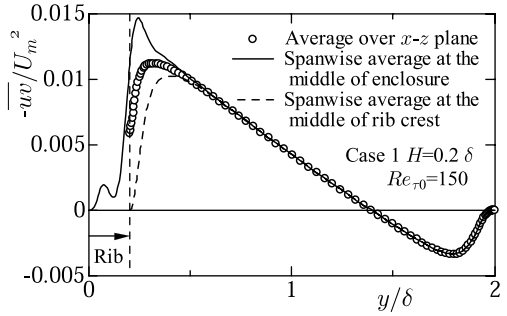

Fig. 10. Profiles of Reynolds shear stress calculated by various ways of averaging.

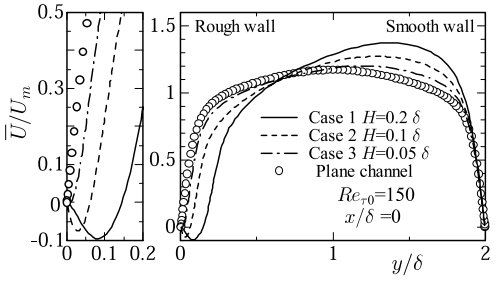

Fig. 11. Profiles of mean velocity.

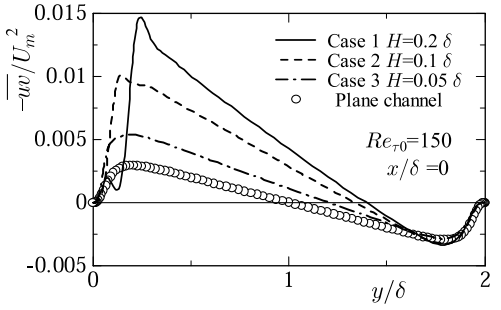

Fig. 12. Profiles of Reynolds shear stress.

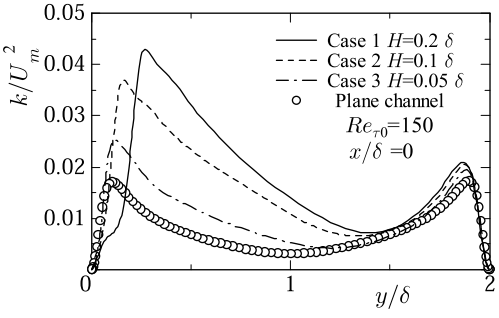

Fig. 13. Profiles of turbulence energy.

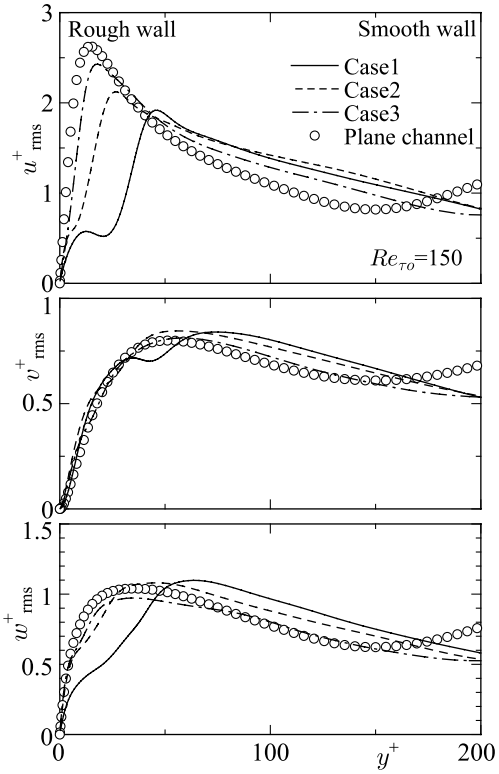

Fig. 14. Distributions of turbulence intensities.

between them is very small; 2.0%, 2.8% and 0.8% of a channel width for Cases 1, 2 and 3, respectively. This might be because the Reynolds number studied is relatively small.

Fig. 14 shows the turbulence intensities normalized by the friction velocity on the rough wall. It is observed that in all cases the statistical quantities get together well in the upper region of the ribs. However, from Fig. 13, it is observed that the turbulence intensities increase relative to the bulk mean velocity. The budget of the turbulence energy is shown in Fig. 15. In Case 1, the convection term is enhanced in comparison with the plane channel flow. This is because the mean vertical velocity component near the rib is increased, and also there is a variation in the turbulence in the streamwise direction. Moreover, the contributions from the turbulent and pressure diffusion terms are very large; in the enclosure between the ribs, there is no turbulence production from the mean shear, but turbulent transport maintains the turbulence there. In Case 3, the distribution of the budget is similar to the result in the plane channel, in comparison with Case 1, but the contributions from the turbulent transport (turbulent and pressure diffusions) are large.

Next, to investigate the anisotropy of turbulence, Fig. 16 shows the pressure–strain correlation terms which are important in the near-wall region. The pressure–strain correlation is affected because the flow impinges on the upstream side of the rib wall, and the pressure fluctuations increase over a wide region on the rough-wall side in comparison with the smooth-wall side. If we compare

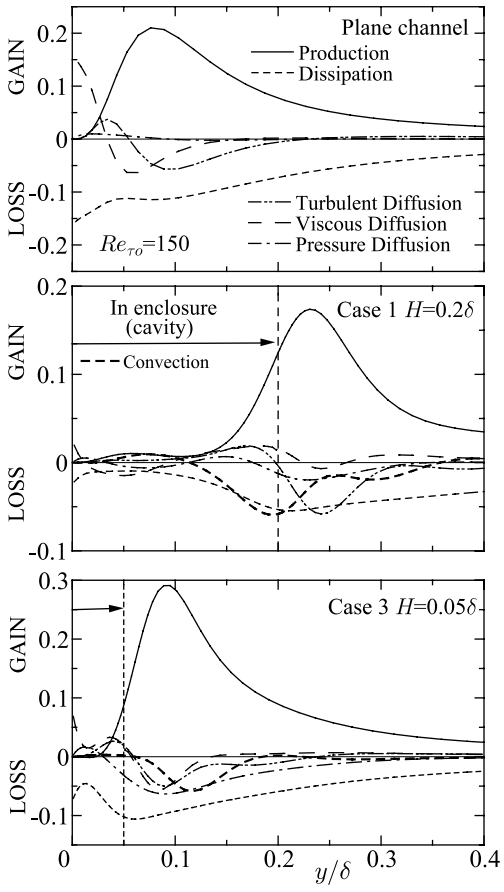

Fig. 15. Budgets of turbulence energy.

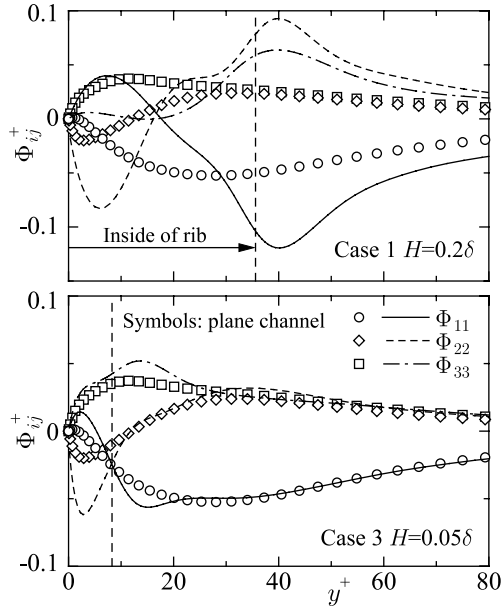

Fig. 16. Distributions of pressure strain terms in transport equations for Reynolds stress.

Case 1, where the rib is highest, with the plane channel flow, the respective components of the pressure–strain term become maximum in the region between the ribs, and a very active energy exchange occurs. In Case 1, the sign of Φ_{11} becomes positive at $y^+ \simeq 15$. In ordinary wall turbulence without external force, it is observed that in the near-wall region, the splatting phenomenon caused by $\overline{v^2}$ gives the energy to $\overline{w^2}$ as seen in the DNS results (Nagano and Hattori, 2003). However, in the enclosure between ribs, the energy does not redistribute to the $\overline{w^2}$ component. This can be attributed to the two-dimensional vortices existing in the enclosure, which promote the redistribution from the $\overline{v^2}$ to $\overline{u^2}$ components. As for Case 3, the effects from the two-dimensional vortex and the reattachment are combined and they affect the redistribution mechanism. This can be considered as the combined result of Case 1 and the plane channel flow. As a result, as shown in Fig. 14, in spite of the existing rough wall, the anisotropy of turbulence shows behavior similar to that in the smooth wall, and the roughness promotes the heat transfer with a relatively small drag.

Finally, Fig. 17 shows the streamwise vortices educed with the second invariant tensors of the velocity gradient II (Kasagi et al., 1995; Iida et al., 2000). In each case, streamwise vortices are produced in the region above the ribs on the rough-wall side, and it is confirmed that the structures spread over the region above the center of the channel. Moreover, if we compare Case 1 with Case 3, many more streamwise vortices are produced in Case 1, where the rib effects are strong. In the enclosure between the ribs, the streamwise vortices are seen in the whole region of the enclosure in Case 3. However, in Case 1, because the flow stagnates downstream of the rib surface, not many streamwise vortices are produced. This corresponds to the results of the distributions of the skin friction coefficient and the Nusselt number as seen in Figs. 7 and 8.

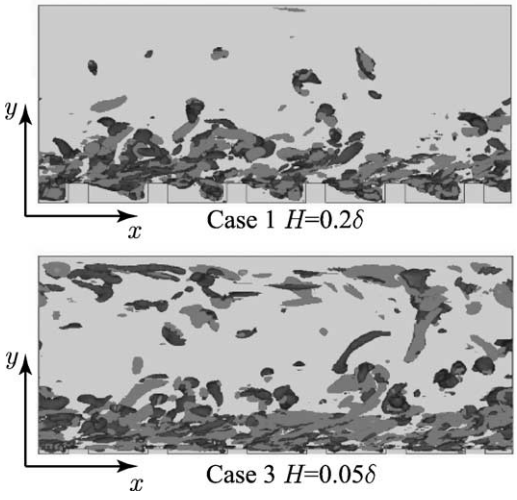

Fig. 17. Vortex structures visualized by second invariant: $II^* < -0.5$.

3.4. Statistical characteristics of thermal field and related turbulent structures

For the thermal field, the turbulence statistics at the middle of the cross-sectional enclosure ($x/\delta = 0$) are discussed below. Fig. 18 shows the mean temperature distribution normalized by the temperature difference ΔT_w. The effect of the rib causes the mean temperature to become asymmetric in all cases as for the mean velocity profiles, and the temperature increases in the major part of the channel. On the other hand, because of the rough-wall effects, the region of the large temperature gradient extends to the smooth-wall side. Fig. 19 shows the turbulent heat flux in the wall-normal direction. The heat transfer is activated from the enclosure with the ribs, but in the thermal field also there are counter gradient diffusions in Case 1. This is because the turbulent heat fluxes are maintained by both the pressure–temperature gradient correlation and turbulent diffusion. However, the production from the mean temperature gradient is not the same as for the Reynolds shear stresses.

Next, Fig. 20 shows the rms intensities of temperature fluctuation, which decrease on the rough-wall side, where the velocity fluctuations are promoted. However, the temperature intensities increase on the smooth-wall side, where the turbulent velocity fluctuation is suppressed. Apparently, the contrary situations occur between the velocity and thermal fields on each side. To investigate the cause and effect, we calculated the production and turbulent diffusion terms of the transport equation for $\overline{\theta^2}/2$ in each case (Fig. 21). The production terms on the smooth-wall side, where the temperature gradient is large and the wall-normal heat fluxes increase, contributes greatly in the region around the peak to the center of the channel. This is why the temperature intensities become large on the smooth-wall side. On the other hand, on the rough-wall side, because the contribution from the production decreases and the turbulence is maintained by the turbulent diffusion, the intensities of temperature fluctuations decrease, especially in Case 1.

In order to examine the relationship between the velocity and thermal fields, the distributions of the turbulent Prandtl number, Pr_t, are shown in Fig. 22. The spanwise averaged Pr_t at the middle of the enclosure and of the rib crest are compared with that in the plane channel flow. Near the region above the rib, Pr_t becomes larger than that on the rib crest. However, it becomes smaller and then becomes larger again in the enclosure. Thus, the turbulent Prandtl number is not constant and the analogy between heat and momentum transfer cannot be expected near the rib roughness. On the other hand, on the smooth-wall side, the Pr_t distribution well corresponds to that in the plane channel flow.

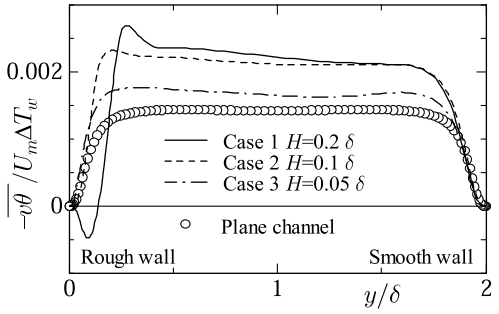

Fig. 19. Profiles of wall-normal turbulent heat flux.

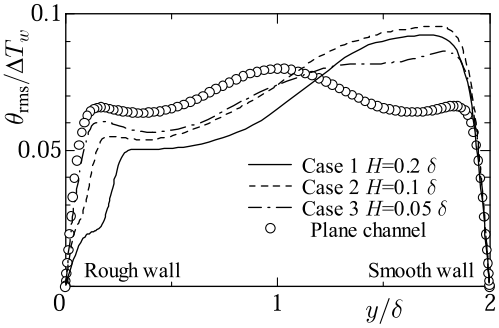

Fig. 20. Profiles of rms intensities of temperature fluctuation.

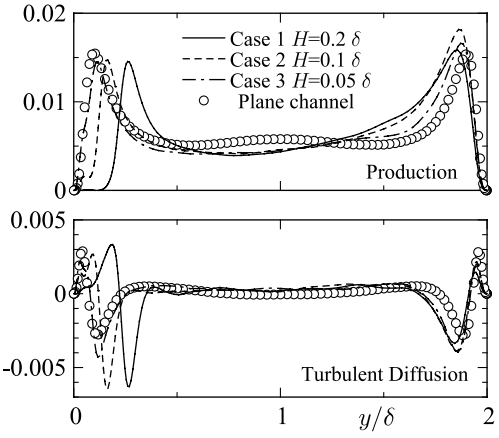

Fig. 21. Production and turbulent diffusion terms in temperature variance budget.

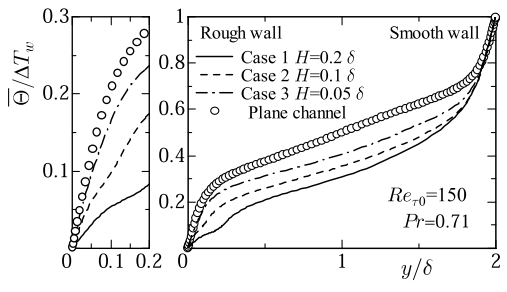

Fig. 18. Profiles of mean temperature.

Finally, to observe the spatial structures which contribute to the transport of the passive scalar, Fig. 23 shows the streamlines, which are spatially averaged along the streamwise direction, and the temperature fluctuations in the y–z cross-section in the plane channel flow and Case 1. In the plane channel flow, the streamlines show the streamwise vortices in the near-wall region, and the sharp variations in temperature fluctuations associate with these vortices. On the other hand, in Case 1 large-scale vortex structures appear, which extend to the center of the channel from the enclosure between the ribs. With this vortex structure, the turbulent mixing becomes larger in the center of the channel, and the turbulence transport is promoted. This behavior is consistent with the above-mentioned statistical results, i.e., the increase in the heat transfer coefficient, the pronounced change in the mean temperature distributions, and the increase in the turbulent diffusion terms in the budget of temperature variance.

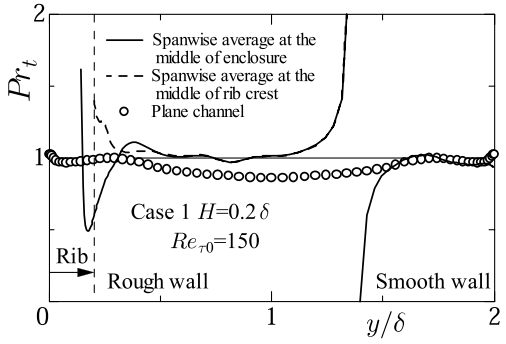

Fig. 22. Turbulent Prandtl number.

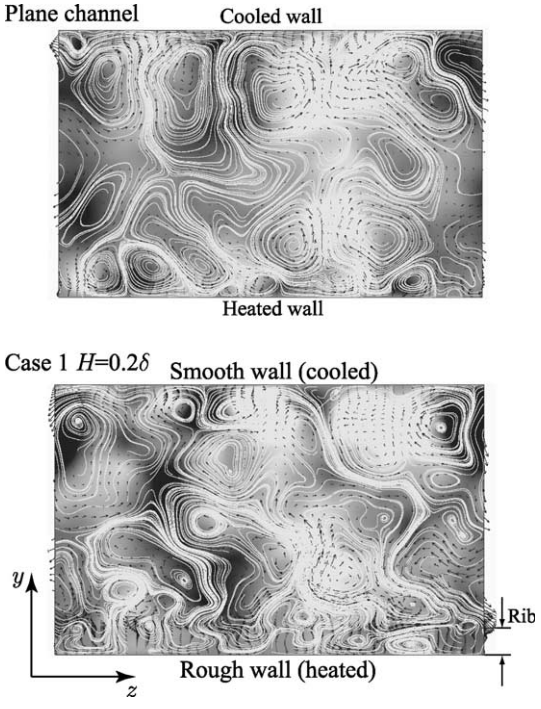

Fig. 23. Streamwise-averaged streamlines and temperature fluctuations in y–z plane: $\theta/\Delta T_w = -0.05$ (white)–0.05 (black).

4. Conclusions

In this study, in order to elucidate the effects of roughness on the statistical quantities in the velocity and thermal fields, direct numerical simulations (DNS) of heat transfer in turbulent channel flows with transverse-rib roughness have been performed by varying their spacing, width and height. The results are summarized as follows.

(1) The Reynolds number differs greatly with the rib arrangement, because of the decrease in the mean velocity, although the pressure gradient is identical with the plane channel flow. For the k-type roughness, heat transfer is promoted by increasing the height of the ribs, but at the same time, the drag increases. This results in a deterioration in heat transfer efficiency compared with the smooth-wall flow. However, with decreasing rib heights, the heat transfer performance can be promoted with a small increase in drag, and the heat transfer characteristic improves. In the d-like type roughness case, however, the heat transfer characteristic cannot be improved regardless of the rib spacing. The heat transfer augmentation is found to be smaller than that in the k-type roughness with the same roughness height.

(2) Because the flow impinges upstream of the rib, the pressure fluctuation becomes larger in the wide region of the rough-wall side. In this situation, turbulence is mainly maintained by the pressure–strain term, and a very active energy exchange occurs between the respective velocity components. The two-dimensional vortices existing in the enclosure promote the redistribution from the $\overline{v^2}$ to $\overline{u^2}$ components. Also, counter-gradient diffusion is observed for the Reynolds shear stress and the wall-normal heat fluxes, and it is confirmed that this results from pressure-related transport terms.

(3) In the enclosure between ribs low in height, the streamwise vortices are seen over the entire region in the enclosure; when the ribs are high, however, the flow stagnates downstream of the ribs and streamwise vortices are not produced. Thus, the local Nusselt number decreases from downstream of the ribs to the center of the enclosure.

(4) Because the higher the rib, the large-scale vortices appear in the center of the channel from the enclosure between the ribs, the turbulent mixing is enhanced and the mean heat transfer coefficient increases, but the drag also increases. Therefore, by arranging the ribs to be lower in height and having the mixing occur in the near-wall region, the overall heat transfer performance becomes very effective including the drag.

Acknowledgements

The authors gratefully acknowledge the support provided for this research by the New Energy and Industrial Technology Development Organization (NEDO) through the Japan Weather Association.

References

Antonia, R.A., Luxton, R.E., 1971. The response of a turbulent boundary layer to a step change in surface roughness. Part 1. Smooth to rough. J. Fluid Mech. 48, 721–761.

Antonia, R.A., Luxton, R.E., 1972. The response of a turbulent boundary layer to a step change in surface roughness. Part 2. Rough to smooth. J. Fluid Mech. 53, 737–757.

Ashrafian, A., Andersson, H.I., 2003. DNS of turbulent flow in a rod-roughened channel. In: Proceedings of the Third International Symposium on Turbulence and Shear Flow Phenomena, Sendai, Japan, vol. 1, pp. 117–122.

Bakken, O.M., Krogstad, P.-Å., 2001. Quadrant analysis of rough and smooth surface channel flow. In: Proceedings of the Second International Symposium on Turbulence and Shear Flow Phenomena, Stockholm, Sweden, vol. 1, pp. 335–340.

Cui, J., Patel, V.C., Lin, C.-L., 2003. Large-Eddy simulation of turbulent flow in a channel with rib roughness. Int. J. Heat Fluid Flow 24, 372–388.

Dean, R.B., 1978. Reynolds number dependence of skin friction and other bulk flow variables in two-dimensional rectangular duct flow. Trans. ASME, J. Fluid Engng. 100, 215–223.

Hanjalić, K., Launder, B.E., 1972. Fully developed asymmetric flow in a plane channel. J. Fluid Mech. 51, 301–335.

Iida, O., Iwatsuki, M., Nagano, Y., 2000. Vortical turbulence structure and transport mechanism in a homogeneous shear flow. Phys. Fluids 12, 2895–2905.

Kasagi, N., Nishimura, M., 1997. Direct numerical simulation of combined forced and natural turbulent convection in a vertical plane channel. Int. J. Heat Fluid Flow 18, 88–99.

Kasagi, N., Sumitani, Y., Suzuki, Y., Iida, O., 1995. Kinematics of the quasi-coherent vortical structure in near-wall turbulence. Int. J. Heat Fluid Flow 16, 2–10.

Kajishima, T., 1999. Finite-difference method for convective terms using non-uniform grid. Trans. JSME (B) 65, 1607–1612, in Japanese.

Kays, W.M., Crawford, M.E., 1993. Convective heat and mass transfer, 3nd ed. McGraw–Hill. pp. 323–325.

Leonardi, S., Orlandi, P., Smalley, R.J., Djenidi, L., Antonia, R.A., 2003. Direct numerical simulations of turbulent channel flow with transverse square bars on one wall. J. Fluid Mech. 491, 229–238.

Liou, T.-M., Hwang, J.-J., Chen, S.-H., 1993. Simulation and measurement of enhanced turbulent heat transfer in a channel with periodic ribs on one principal wall. Int. J. Heat Mass Transfer 36, 507–517.

Miyake, Y., Tsujimoto, K., Nakaji, M., 2000. Direct numerical simulations of rough-wall heat transfer in a turbulent channel flow. Int. J. Heat Fluid Flow 22, 237–244.

Nagano, Y., Hattori, H., 2003. DNS and modelling of spanwise rotating channel flow with heat transfer. J. Turbul. 4 (1), 1–15.

Perry, A.E., Schofield, W.H., Joubert, P.N., 1969. Rough wall turbulent boundary layers. J. Fluid Mech. 37, 383–413.

Townsend, A.A., 1976. The structure of turbulent shear flow, 2nd ed. Cambridge University Press, Cambridge. pp. 139–143.

Vogel, J.C., Eaton, J.K., 1985. Combined heat transfer and fluid dynamic measurements downstream of a backward-facing step. Trans. ASME, J. Heat Transfer 107, 922–929.